Distributed Voltage Control of Energy Storage Systems Combined with Electric Springs in the Presence of Cyber-Attacks

Yajie Jiang, *Member, IEEE*, Xiangrong Zhang, Yici Wang, Yunjie Gu, *Senior Member, IEEE*, Eric Ka-wai Cheng, *Fellow, IEEE*, and Yun Yang, *Senior Member, IEEE*

***Abstract*—Given the unpredictable nature of renewable energy injection, a combination of second-life batteries and three-phase electric springs (ESs) is utilized to stabilize the bus voltage from the load side. Voltage stability for critical loads is achieved through the use of a voltage feedback-based reactive power regulation strategy, which makes effective use of the limited output current provided by the second-life batteries. In addition, a consensus algorithm is introduced to facilitate information sharing among multiple ESs, thereby ensuring voltage consensus and restoration. However, the consensus controller is exposed to the risk of false data injection (FDI) attacks, which could lead to voltage fluctuations in the converters. To address this issue, a distributed high-order differentiator (DHOD) is proposed, characterized by its fast response speed and high estimation accuracy, to detect and eliminate attack signals. Through both simulation and experimental validation, it is demonstrated that the proposed strategy enhances voltage stability and energy throughput, even when subjected to FDI attacks.**

***Index Terms*—Distributed high-order differentiator (DHOD), false data injection (FDI) attack, three-phase electric springs (ESs), second-life battery.**

I. INTRODUCTION

Secondary batteries, which are electric vehicle battery packs that have reached their end-of-life for vehicular use but still possess adequate performance, can be repurposed for other applications [1] - [3]. Despite their reduced capacities, these second-life batteries provide substantial benefits, particularly in stationary energy storage systems in electric networks. To improve energy systems and optimize material utilization, these batteries can be integrated into smart grid systems for functions such as load leveling and addressing power needs in residential or commercial settings [4]. However, it is important to acknowledge that second-life lithium-ion batteries may have limitations in output current and power. These limitations arise from factors such as internal degradation, cell imbalance, and increased internal resistance over time. Therefore, to effectively utilize these batteries, they should be deployed in applications with lower power output requirements and combined with appropriate control methods to optimize their performance [5].

Recently, electric springs (ESs) have been widely used to regulate power flow and suppress voltage deviations at the point of common coupling (PCC), helping to mitigate the challenges posed by the intermittent integration of renewable energy sources (RESs) [6]. The ESs have proven effective in addressing three-phase imbalances [7] and mitigating voltage fluctuations [8] resulting from the integration of non-adjustable RESs. Under normal operation, ESs can be equivalent to a controlled voltage source with adjustable amplitude and phase for the power grid [9]. Through appropriate control strategies, the voltage across non-critical loads (NCLs) and the currents consumed by these loads can be directly changed, thereby indirectly altering the active and reactive power flows on the load side [10]. In this way, ESs adjust the voltage and power of non-critical loads (NCLs) while simultaneously enhancing the voltage and power quality of critical loads (CLs) [11]. Through the combination of ESs with NCLs, the smart load (SL) can be formed, enabling multiple functionalities such as load-side voltage restoration, and static VAR compensation, without the need for hardware modifications.

ESs can be classified into three main types: ES with capacitor (ES-I) [12], ES with batteries (ES-II) [13], and back-to back ES (ES-B2B) [14]. Control strategies for ESs leverage phase-locked loops (PLLs) to regulate the instantaneous phase angle and voltage amplitude, thereby achieving voltage restoration and power compensation [14]. These strategies include δ-control and radial-chordal decomposition control. In the current grid-connected control systems for three-phase ESs, the system relies on phase detection links to monitor and adjust the voltage angle of the grid. This control setup characterizes the ES as a unit that follows the grid, similar to a controlled current source. Inspired by PQ control strategies, a simpler power control approach has been proposed, which reduces parameter dependency [15]. Moreover, research in [9] explores the adjustment of controller parameters for multiple ESs to enhance overall system stability in weak power grids. While these control strategies effectively adjust the ES to ensure load-side voltage stability and power balance, they have notable drawbacks, such as slow dynamic response speed and parameter dependence.

In order to balance the simplicity of the structure and the flexibility of power regulation, the ES-II combined with second life batteries is applied for voltage regulation in RES-based microgrids. The proposed ES-II can provide active power and reactive power for maintaining high-quality frequency and voltage. The effectiveness of the ES-II system is improved through the implementation of a global tuning scheme, as discussed in [16]. This scheme focuses on adjusting the tuning coefficients of local controllers within ES-II to ensure the stable voltage and frequency operation of microgrids without the need for communications. Furthermore, [17] introduces a federated learning scheme that offers references for local controllers to achieve precise control and improve dynamic response. To address voltage and frequency fluctuations within microgrids, [18] suggests controlling multiple ES using a consensus-based droop control approach. Additionally, it investigates consensus control among groups of ESs through communication layers to further address these challenges [19]. This strategy aims to collectively mitigate fluctuations in both voltage and frequency for enhanced stability and efficiency in microgrid operations.

For distributed energy resources and ESs, the consensus algorithm is a key tool that enhances system stability by facilitating voltage and frequency recovery control. However, a significant challenge arises in ensuring the security of data exchange among neighboring nodes due to the risk of false data injection (FDI) attacks [20]. The vulnerability of AC electric networks to such attacks arises from their reliance on communication networks and the prevalence of software-driven controllers, which leave them susceptible to malicious network intrusions [21], [22]. The potential consequences of FDI attacks include disruptions to normal system operations, which can lead to system instability and power supply interruptions. In response to this threat, previous studies have focused on developing adaptive control strategies designed to detect and mitigate the adverse effects of false information [23]. Various methods have been proposed for detecting attack signals and regulating load-side voltage, including index-based detection, neural network mapping, and state observation [24].

A sliding mode utilizes observer-based secondary control to detect and compensate for attack signals. Recognizing the significant impact of FDI attacks, it has been proposed that these attack signals at the secondary controller be treated as additional disturbances within the dynamic system [25]. In response, an observer-based compound secondary control mechanism has been developed. This mechanism estimates the specific waveform of the attack signal and counteracts its effects through appropriate compensation [26], [27]. Despite these advancements, first-order observers have inherent limitations, such as inadequate signal-tracking dynamics and the potential introduction of noise when response speed is increased [28]. Furthermore, the application of observation techniques and FDI attacks within the context of the average consensus algorithm—a widely used method—remains largely unexplored [29]. Addressing these challenges and enhancing the resilience of grid-connected systems against FDI attacks is crucial for ensuring the reliable and secure operation of microgrids amid evolving cybersecurity threats [30].

In order to fully recycle and utilize secondary batteries, based on the characteristics of limited output current, secondary batteries are combined with inverters to be used as ESs. We optimize the limited output current of second-life batteries using a voltage feedback-based reactive power regulation approach, ensuring voltage stability on CLs. Additionally, by implementing a consensus algorithm, multiple ES units can achieve voltage consensus and restoration, even when facing potential FDI attacks on the consensus controller. To address this vulnerability, we propose a distributed high-order differentiator (DHOD) for detecting and eliminating attack signals. Simulation and experimental validation show that our approach effectively enhances voltage stability and energy throughput, even in the presence of network attacks, thereby reinforcing the system's resilience against potential threats. The main contribution of this paper can be summarized as:

1) To enhance voltage robustness against power variations (by RES), a voltage regulator is designed to generate the reactive power reference.
2) This paper develops a distributed differentiator designed to detect FDI attacks on multiple ESs (SLs) and address these attack signals through a distributed consensus control strategy.

II. THREE-PHASE ES AND CONSENSUS CONTROL

A. *System Configuration*

The aging of lithium-ion batteries is a complex process influenced by multiple factors. The main causes include: deep discharging/charging, high-temperature, and mechanical stress [31]. These aging factors have a significant impact on the battery's output current. As the battery ages, its internal resistance gradually increases, leading to higher internal resistance and thus affecting the battery's output current. High internal resistance can prevent the battery from providing stable current under high load conditions, resulting in decreased power output capability. Additionally, aging reduces the battery's capacity, causing the actual output current to be significantly lower than that of a new battery under the same discharge conditions. This decrease in current not only affects battery performance but may also lead to system instability or restricted device functionality. To make more use of aging or retired power batteries, this article studies the voltage collaborative control of multiple ESs simultaneously connected to power grid. A typical three-phase system with SL_i and ES_i is plotted in Fig. 1. The ES_i is linked to the NCL_i through the capacitors. Specially, $Z_{\mathrm{CL}i}$ and $Z_{\mathrm{NCL}i}$ represent the impedances of CL_i and NCL_i, respectively. Based on the sampled phase angle, currents and voltages, the converter of ES_i is regulated by using PLL and control loops. To realize power compensation, the control scheme comprises an outer power loop and an inner voltage-current loop. The given active power ($P_{\mathrm{ref}i}$) and reactive power ($Q_{\mathrm{ref}i}$) are adopted in the power control loop. The primary-level control of SL_i is devoted to regulating the local current by tracking the reference points generated by upper-level control.

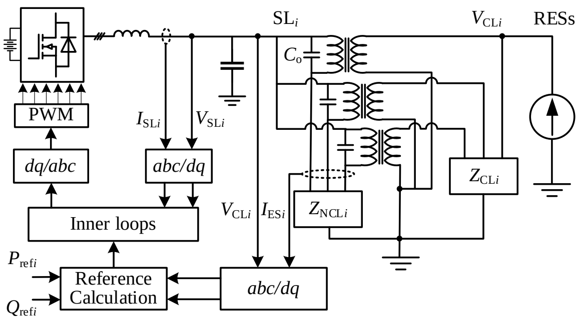

Fig. 1. A three-phase AC microgrid with ES-based SLs.

By taking the ES_i as an example, the voltage vector control of a single ES is introduced here. The equivalent circuit of ES_i is shown in Fig. 1. The SL_i, formed by ES_i and its associated network control load NCL_i, is connected to the local bus in a distribution feeder. This SL is then connected in parallel with the critical load CL_i. When the power injected by distributed RES exceeds the rated capacity of the load, a large amount of reactive power is generated, resulting in over-voltage on the critical loads. In this situation, the ESs need to provide capacitive reactive power, causing the current to lead the voltage. Conversely, when the power injected by distributed

RES is less than the rated capacity of the load, insufficient current can cause under-voltage on the CLs. In this case, the ESs must provide inductive reactive power, making the current lag behind the voltage. For ES-II, which incorporates a battery, the ES can generate both active and reactive power due to the battery's auxiliary effect.

The CL's voltage ($V_{\mathrm{CL}i}$), ES' voltage ($V_{\mathrm{ES}i}$), and the NCL's voltage ($V_{\mathrm{NCL}i}$) always form a triangle. As $V_{\mathrm{NCL}i}$ depends on the impedance of NCL$_i$, ES' current ($I_{\mathrm{ES}i}$) is equal to NCL's current ($I_{\mathrm{NCL}i}$), given as

$$V_{\mathrm{CL}i} = V_{\mathrm{ES}i} + V_{\mathrm{NCL}i} \quad (1) \qquad I_{\mathrm{ES}i} = I_{\mathrm{NCL}i} \quad (2)$$

With a properly designed control strategy, the voltage of the ES$_i$, $V_{\mathrm{ES}i}$ can be regulated to stabilize the voltage of the CL$_i$, $V_{\mathrm{CL}i}$ at its nominal value. Typically, the control of ESs involves phase-detection methods, such as radial chordal decomposition (RCD) control and δ-control schemes. However, these strategies are not compatible with traditional grid-connected inverters and hinder the broader adoption and application of ESs. This work seeks to apply power regulation strategy for voltage stabilization among CLs, NCLs, and ESs. In practical applications, the uncertainty associated with injected renewable energy makes it challenging to directly calculate accurate power reference values. Consequently, inappropriate power reference values can prevent the voltage vector output by the ESs from aligning with the voltage vector of NCLs, leading to either over-voltage or under-voltage conditions on CLs. This issue is illustrated by the simplified voltage vector diagram of ES$_i$, NCL$_i$, and CL$_i$, as shown in Fig. 2.

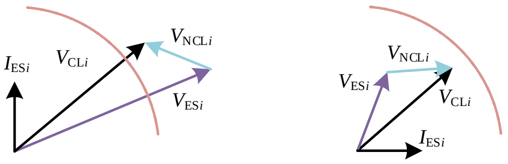

(a) (b)

Fig. 2. Voltage vectors under mismatched powers: (a) capacitive reactive power compensation by ESs, (b) inductive reactive power compensation by ESs.

B. *Voltage Restoration Control*

Integration of RES into the power grid can cause voltage fluctuations due to active/reactive power shortages. To address this issue, a consensus-based secondary voltage control strategy has been proposed to stabilize the system voltage. This strategy involves two main layers for each SL: an inner loop for current control to regulate three-phase ESs, and an outer loop for consensus control to generate reference voltages. The consensus control allows each SL to access local voltage information and exchange data in a distributed manner without requiring global communication. The consensus algorithm ensures that each SL updates its information based on the states of neighboring SLs, aiming for all SLs to converge to a common voltage value. Fig. 3 depicts a three-phase system with multiple SLs and ESs. Note that the line resistances and reactance within the electric system are ignored for illustration.

From the view of cyber-layer, the topology can be abstracted as a graph with n SLs. Each SL can exchange its voltage with its neighbors. From the view of graph, $\boldsymbol{A}$ is defined as the adjacency matrix, and $\boldsymbol{L}$ represents the Laplacian matrix. In details, a_{ij} is the element: $a_{ij} > 0$ indicates SL$_i$ can receive information from SL$_j$, $a_{ij} = 0$ otherwise. Here, one intermediate variable of SL$_i$ is defined as

$$x_i = V_{CLi} \tag{3}$$

By adopting the average consensus protocol, the state variables of SLs, voltages, can be synthesized as x_i. Then, the iterative form of the state variables in the discrete domain can be derived as

$$x_i(k+1) = x_i(k) + \varepsilon * \{\textstyle\sum_{j\in n_i}^{n} a^{ij}\left[x_j(k) - x_i(k)\right] + g_i\left(x_{\mathrm{ref}} - x_i(k)\right)\} \tag{4}$$

where x_j is the inter-media variable from node j, ε is the edge weight used for tuning the dynamics of the consensus algorithm. g_i is the voltage regulation coefficient [24]. By adopting the consensus dynamics in (4), the state variables of ESs will be converged as

$$\lim_{t\to\infty} \left\| x_i(t) - x_j(t) \right\| = 0 \tag{5}$$

To minimize the state-variable convergence time in communication graph, the value of ε is adjusted to be:

$$\varepsilon = 2/[\lambda_1(\boldsymbol{L}) + \lambda_{n-1}(\boldsymbol{L})] \tag{6}$$

where $\boldsymbol{L}$ is the Laplacian matrix. $\lambda_{n-1}(\boldsymbol{L})$ is its second smallest eigenvalue of $\boldsymbol{L}$, and $\lambda_1(\boldsymbol{L})$ is its largest eigenvalue $\boldsymbol{L}$.

Based on (4), the secondary control for voltage restorations can be derived as

$$V_{\mathrm{ref}i} = V_{\mathrm{nom}} + \delta_{Vi} \quad (7.1) \qquad \dot{\delta}_i = u_i = x_i - V_{CLi} \quad (7.2)$$

where δ_i is the adaptive voltage term for voltage restoration of the SL$_i$. u_i is the control input for voltage regulations of the SL$_i$. $V_{\mathrm{ref}i}$ and V_{nom} are the reference value and nominal value of voltage. With the help of distributed communication topology, the adaptive voltage terms can be generated by the integrations in (7) when the consensus is achieved.

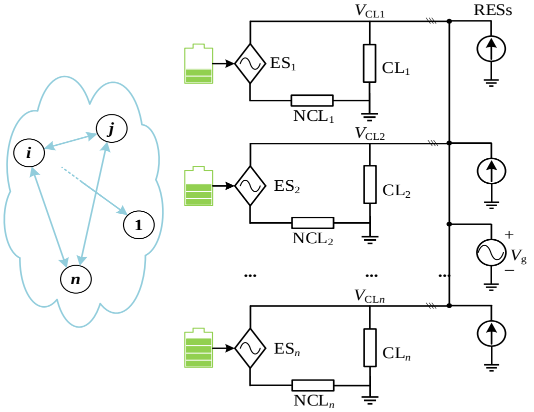

Fig. 3. Schematic diagram of SL collaborative operation.

To enhance the voltage regulation performance against load power variations, this article adopts voltage feedback regulation to generate reactive power reference values:

$$Q_{\mathrm{ref}\,i} = (k_{VPi} + \frac{k_{VIi}}{s})(V_{\mathrm{ref}i} - V_{\mathrm{CL}i}) \tag{8}$$

where k_{VPi}, and k_{VIi} are the gains of controllers, $Q_{\mathrm{ref}i}$ is the reactive power reference value of ES$_i$. Moreover, the reactive power compensation error is implemented as

$$e_{Qi} = (Q_{\mathrm{ref}i} - Q_i) \tag{9}$$

Moreover, another secondary voltage compensation term is implemented as

$$V_{adp\,i} = (k_{QPi} + \frac{k_{QIi}}{s})e_{Qi} \tag{10}$$

where k_{QPi}, and k_{QIi} are the gains of controllers. Thus, the final secondary control is formed as

$$V_{\mathrm{ref}i} = V_{\mathrm{nom}} + V_{adp\,i} + u_i \tag{11}$$

The logic of the control strategy in (11) is that in the case of mismatched new energy injection, the voltage on the critical load is determined by the reactive power compensated by the power spring. The detailed control diagram in this paper is plotted in Fig. 4. Specially, the voltage phase angle θ required for coordinate transformation in the figure is obtained through a phase-locked loop. By utilizing the reference voltage, the reactive power reference can be dynamically determined for voltage regulation, and the active power can also be adjusted adaptively. The matched voltage vector diagram of ES$_i$, NCL$_i$, and CL$_i$, is plotted in Fig. 5.

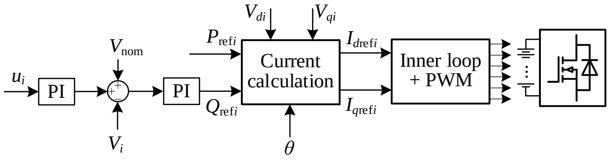

Fig. 4. Control diagram of ESs.

(a) (b)

Fig. 5. Voltage vectors under matched powers: (a) capacitive reactive power compensation by ES, (b) inductive reactive power compensation by ES.

III. DHOD-BASED CONSENSUS CONTROL STRATEGY

A. Analysis of FDI Attacks

The state variable x_i is designed to facilitate the exchange of voltage information (i.e., $V_{\text{SL}i}$) in this paper. Considering the secondary control layer, the system dynamics are analyzed as a cyber-physical system. Consequently, a first-order model is employed for the subsequent analysis. Attack signals with different values (waveforms) are directly applied to the consensus-based secondary controller. For consensus-based hierarchical control, as shown in Fig. 5, the control inputs with the FDI signal can be written as

$$V_{\text{ref}i} = V_{\text{nom}} + V_{adp\,i} + \delta_i' \quad (12.1) \qquad \dot{\delta}_i' = u_i + \eta_i \quad (12.2)$$

where δ_i' denotes the incorrect FDI attack signal. η_i represents the attack signal on the secondary controller of SL$_i$. This signal can be a finite step signal, a sinusoidal signal, a ramp signal, or a combination of these types. FDI attacks interfere with the feedback control variables of secondary layers, leading to voltage fluctuations and power imbalances.

To evaluate the attack effect, it is assumed the virtual reference nodes exist in the network system. Meanwhile, the reference variables are defined as $x_{\text{ref}} = V_{\text{ref}}$ for consensus-based voltage regulation. During consensus process, the tracking error of the inter-mediate variable x_i is defined as

$$e_i(t) = x_i(t) - x_{\text{ref}} \quad (13)$$

Based on (4), the dynamics of x_i can be derived as

$$\dot{x}_i = \varepsilon * \left[\textstyle\sum_{j\in n_i}^{n} a_{ij}\left(x_j - x_i\right) + g_i(x_{\text{ref}} - x_i)\right] \quad (14)$$

As the FDI attack is applied, the system dynamics can be transformed as a first-order system with disturbance as

$$\dot{x}_i = \varepsilon * u_i + \eta_i \quad (15)$$

where the attack signal and its derivatives are bounded as

$$|\eta_i(t)| \in [0, \xi] \quad (16.1) \qquad |\dot{\eta}_i(t)| \in [0, \zeta] \quad (16.2)$$

where ξ and ζ are the corresponding maximum values that can be determined based on the electric network topologies, system parameters, control parameters, etc.

B. Design of DHOD

Generally, the time constant of local control is much smaller than that of secondary layer control in an ES system. According to [4], incorporating output voltages into a control variable x_i allows for the characterization of ES system dynamics using system-level modeling. Building on the analysis of distributed secondary control under FDI attacks, a DHOD-based hierarchical control is designed to monitor and compensate for these attacks. Once consensus is reached, the edge weight ε can be disregarded. Consequently, the dynamics of the SLs under FDI attacks can be expressed as follows:

$$\dot{x}_i(t) = B_i u_i(t) + B_i \eta_i(t) \quad (17.1)$$

$$y_i(t) = x_i(t) \quad (17.2)$$

where B_i is a coefficient for secondary controller. By defining x_{1i} as x_i, x_{2i} as η_i, and x_{3i} as $\dot{\eta}_i$, the extended state dynamics can be written as

$$\dot{x}_{1i}(t) = B_i u_i(t) + B_i x_{2i}(t) \quad (18.1)$$

$$\dot{x}_{2i}(t) = x_{3i}(t) \quad (18.2) \qquad \dot{x}_{3i}(t) = \dot{\eta}_i(t) \quad (18.3)$$

In the following analysis, we define $\boldsymbol{G}$ = diag(g_1, g_2,…, g_n). Meanwhile, the effect of B_i is ignored, as it only affects the dynamic response speed and does not influence the steady-state error [32]. To analyze the destructive effects of FDI attack, we introduce the following lemma.

Lemma 1: If the directed graph has a spanning tree and at least one root node, then the matrix $\boldsymbol{L} + \boldsymbol{G}$ is non-singular and positive definite.

The voltage state error e_i is defined as the difference between V_i and the reference value V_{ref}. Then, the voltage state error containing n ESs under attack is expressed with FDI attacks, yields the vector of error dynamics

$$\dot{\boldsymbol{e}} = -\boldsymbol{\varepsilon}(\boldsymbol{L} + \boldsymbol{G})\boldsymbol{e} + \boldsymbol{\eta} \quad (19)$$

where $\boldsymbol{e} = [e_1, e_2, \ldots, e_n]^{\mathrm{T}}$, $\boldsymbol{\eta} = [\eta_1, \eta_2, \ldots, \eta_n]^{\mathrm{T}}$, $\boldsymbol{\varepsilon}$ = diag(ε_1, ε_2, …, ε_n), and. Without loss of generality, the amplitude of the attack signal has a steady-state value, i.e., $\eta(\tau) > \eta_0$. According to (19), the dynamic voltage tracking error (in time-domain) can be obtained as

$$\boldsymbol{e}(t) = \exp^{-\boldsymbol{\varepsilon}(\boldsymbol{L}+\boldsymbol{G})t}\boldsymbol{e}(t_0) + \textstyle\int_{t_0}^{t} \exp^{-\boldsymbol{\varepsilon}(\boldsymbol{L}+\boldsymbol{G})(t-\tau)}\boldsymbol{\eta}(\tau)d\tau \quad (20)$$

where exp is the exponential function, and from Lemma 1 it follows that $-(\boldsymbol{L} + \boldsymbol{G})$ is negative definite and invertible. Under the condition of

$$\lim_{t\to\infty} \exp^{-\boldsymbol{\varepsilon}(\boldsymbol{L}+\boldsymbol{G})t}\boldsymbol{e}(t_0) = 0 \quad (21)$$

the first term in (20) converges to zero. Meanwhile, the second term in (20) fails to converge to zero, as expressed by

$$\begin{aligned} \lim_{t\to\infty} \boldsymbol{e}(t) &= \lim_{t\to\infty} \int_{t_0}^{t} \exp^{-\boldsymbol{\varepsilon}(\boldsymbol{L}+\boldsymbol{G})(t-\tau)}\boldsymbol{\eta}(\tau)d\tau \\ \geq * \lim_{t\to\infty} \exp^{-\boldsymbol{\varepsilon}(\boldsymbol{L}+\boldsymbol{G})t}&\left[\exp^{\boldsymbol{\varepsilon}(\boldsymbol{L}+\boldsymbol{G})t} - \exp^{\boldsymbol{\varepsilon}(\boldsymbol{L}+\boldsymbol{G})t_0}\right][\boldsymbol{\varepsilon}(\boldsymbol{L}+\boldsymbol{G})]^{-1}\eta_0 \\ &= [\boldsymbol{\varepsilon}(\boldsymbol{L}+\boldsymbol{G})]^{-1}\eta_0 > 0 \quad (22) \end{aligned}$$

Here, (21) and (22) show that injecting an attack signal into the secondary controller prevents the system state variable from converging, causing the state-variable error to persist and obstructing current distribution and loss optimization goals. Thus, traditional secondary voltage control cannot achieve its objectives after attacks, undermining system stability.

According to the observation theory, the state variable x_i and attack signals are observable. Here, a DHOD is proposed to detect the FDI attacks as

$$\begin{gathered}\dot{z}_{1i}(t) = B_i u_i(t) + B_i z_{2i}(t) - B_i K_1 |e_{1i}(t)|^{\frac{2}{3}} sign[e_{1i}(t)] \\ \dot{z}_{2i}(t) = z_{3i}(t) - K_2 |e_{1i}(t)|^{\frac{1}{3}} sign[e_{1i}(t)] \\ \dot{z}_{3i}(t) = -K_3 sign[e_{1i}(t)]\end{gathered} \tag{23}$$

where $z_{1i}(t)$, $z_{2i}(t)$ and $z_{3i}(t)$ are the estimated state variables of $x_i(t)$, $\eta_i(t)$, and $\dot{\eta}_i(t)$, respectively. K_1, K_2, and K_3 are the coefficients of DHOD.

From (23), the observation error of x_{1i} is

$$e_{1i}(t) = z_{1i}(t) - x_{1i} \tag{24}$$

When the controller of SL_i encounters an attack, the estimated state variables fail to accurately track the measured ones, leading to a non-zero estimation error $e_{1i}(t)$. This error reflects the differences in state variables between neighboring nodes. The attack signal can be inferred through the integral operation of DHOD as $z_{1i}(t)$ according to equation (23). By monitoring these attack signals, FDI attacks can be mitigated through compensation within the feed-forward loop of the consensus-based secondary controller. Notably, DHOD functions as a high-order observer, providing superior dynamic response and robustness compared to conventional first-order observers.

In a network system, the state variables of each node are inter-connected with those of other nodes, implying that attack signals may be detected by the DHOD even at nodes that haven't been directly attacked. To discern the attacked nodes, the following rules are considered in this paper:

1) If the output of one SL is observed to be zero, the controller is deemed immune from FDI attacks.
2) If one SL's output is non-zero and exactly two SLs show non-zero outputs, the falsified SL is further identified based on the output voltages. If the output voltage increases, the SL with a positive observation output is identified as attacked. Conversely, if the output voltage decreases, the SL with a negative observation output is identified as attacked. The amplitude of attack signal is
$$\hat{\eta}_i(t) = \frac{z_{2i}(t)}{B_i} \tag{25.1}$$
3) If the output of one SL is observed to be non-zero and the number of non-zero SLs exceeds two, the falsified SL can be identified by finding the one that is connected to all other nodes except itself. The amplitude of the attack signal is
$$\hat{\eta}_i(t) = \frac{z_{2i}(t)}{n_{Gi} * B_i} \tag{25.2}$$

where n_{Gi} represents the neighboring SLs of SL_i. For other SLs, although the state variables can be estimated, the identified attack signals are zero. The estimated attacks detected by DHOD will be adopted for controller compensation. The control inputs of the secondary control with DHOD can be written as

$$u_i' = x_{Vi}(k) - V_i - \hat{\eta}_i(t) \tag{26}$$

The block diagram of the proposed DHOD-based hierarchical control is depicted in Fig. 6, illustrating the control design for multi-ES. This design comprises two layers: the upper layer involves DHOD-based cooperative control, while the lower layer focuses on voltage-current control. Through a distributed data-exchanging scheme, the consensus secondary control provides adaptive voltages for the current/power loop, subsequently modulated to offer voltage references for the local loop. In the event of a distributed cooperative controller attack, the DHOD estimates the attack signal for controller compensation, thereby enhancing system voltage stability.

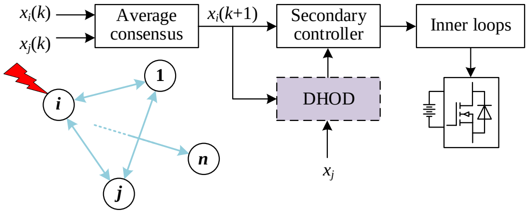

Fig. 6. Schematic diagram of FDI attack on SL_i in a three-phase system.

C. *Convergence Analysis of DHOD*

To analyze the convergence of DHOD, its coefficients, i.e., K_1, K_2, K_3 are defined as:

$$K_1 = 3k, K_2 = 2k^2, K_3 = \left(\tfrac{2}{3}\right)^2 k^3 \tag{27}$$

Notice that the gains of the observer are parameterized in terms of only one parameter $\kappa > 0$ sufficiently large. In general, the observed variables can easily follow the system state variables. To analyze DHOD in (23), the observation errors are defined as

$$\begin{gathered}e_{1i}(t) = z_{1i}(t) - x_i(t) \\ e_{2i}(t) = z_{2i}(t) - d_i(t) \\ e_{3i}(t) = z_{3i}(t) - \dot{d}_i(t)\end{gathered} \tag{28}$$

In the following stability analysis, the parameter B_i can be ignored. Combining with system dynamics, the derivatives of the observation errors are given as

$$\begin{gathered}\dot{e}_{1i}(t) = e_{2i}(t) - K_1 |e_{1i}(t)|^{\frac{2}{3}} \mathrm{sign}[e_{1i}(t)] \\ \dot{e}_{2i}(t) = e_{3i}(t) - K_2 |e_{1i}(t)|^{\frac{1}{3}} \mathrm{sign}[e_{1i}(t)] \\ \dot{e}_{3i}(t) = \dot{d}_i(t) - K_3 \mathrm{sign}[e_{1i}(t)]\end{gathered} \tag{29}$$

Three variables are defined as follows:

$$\xi_1 = |e_{1i}(t)|^{\frac{2}{3}} \mathrm{sign}[e_{1i}(t)], \xi_2 = \frac{e_{2i}(t)}{k}, \xi_3 = \frac{3}{2k^2} e_{3i}(t) |e_{1i}(t)|^{\frac{1}{3}} \tag{30}$$

By denoting the error vector as $\boldsymbol{\xi} = [\xi_1 \quad \xi_2 \quad \xi_3]^T$, the compact form of (30) can be given as

$$\boldsymbol{\xi} = \frac{2k}{3|e_{1i}(t)|^{\frac{1}{3}}} [(\boldsymbol{A} - \boldsymbol{S}^{-1} \boldsymbol{C}^T \boldsymbol{C}) + \boldsymbol{\Phi}_0] \tag{31}$$

where $\boldsymbol{A} - \boldsymbol{S}^{-1} \boldsymbol{C}^T \boldsymbol{C} = \begin{bmatrix} -3 & 1 & 0 \\ -3 & 0 & 1 \\ -1 & 0 & 0 \end{bmatrix}$, $\boldsymbol{C} = [1 \quad 0 \quad 0]$, and

$$\boldsymbol{\Phi}_0 = \begin{bmatrix} 0 \\ 0 \\ \frac{3\dot{d}_i(t)}{2k^3} |e_{1i}(t)|^{\frac{1}{3}} + \frac{\xi_3}{2k|e_{1i}(t)|^{\frac{2}{3}}} (-3\xi_1 + \xi_2) \end{bmatrix}$$

Assumption 1: With respect to the state-variable and control input, the function $\boldsymbol{\Phi}_0$ is continuous locally Lipschitz. In other words, it can be found a positive constant β such that $\|\boldsymbol{\Phi}_0\| \leq \beta \|\xi\|$.

Combining with the AC electric system, and Assumptions 1 are satisfied: by the DHOD, the estimation error of (29) converges to zero in finite time, i.e., $e_{1i} = e_{2i} = e_{3i} = 0$. Thus, by using the DHOD, the estimated attack signal will converge to the real value asymptotically.

IV. Case Studies

To verify the DHOD-based distributed consensus control strategy, a five-bus AC electric network with three SLs is established. This network is based on a standard five-bus power system, with the addition of seven-line impedances. The physical layer of this setup is implemented using MATLAB/Simulink and the OPAL-RT platform, as shown in Fig. 7(a). Three SLs are connected to three of the buses, while two additional loads are connected to the remaining buses. Each SL includes an ES, a CL, an NCL, and a RES unit. Each ES is composed of an aging battery-based distributed energy storage unit and a power converter. The main parameters for the ESs, loads, and the AC network are detailed in Table I. The communication topologies for the various cases are illustrated in Fig. 7(b).

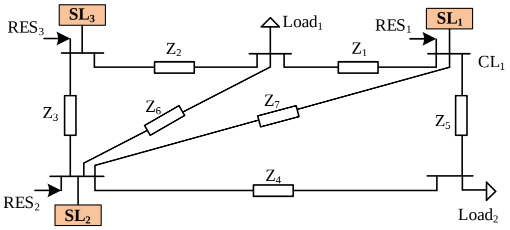

(a) AC microgrid structure

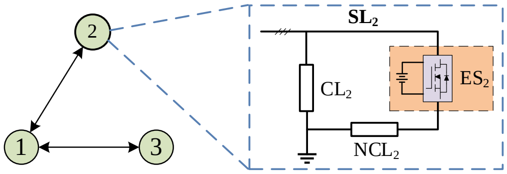

(b) Communication network

Fig. 7. One five-bus AC system with three SLs.

TABLE I. Parameters of the AC Microgrid and ESs

Parameters	**Value**
Nominal bus voltage	220 V
Lower limit of the AC bus voltage	209 V
Upper limit of the AC bus voltage	231 V
Nominal frequency	50 Hz
Current amplitude of RES$_1$	30A
Current amplitude of RES$_2$	32A
Current amplitude of RES$_3$	30A
Impedance of NCLs	40Ω + 0.05H
Rated load of CLs	6000W + 4000Var
Capacity of Load$_1$	1200W + 600Var
Capacity of Load$_2$	1000W + 400Var
Wire impedance of $Z_1 = R_1 + jX_1$	1.2730 + j0.1655 Ω
Wire impedance of $Z_2 = R_2 + jX_2$	0.6365 + j0.08275 Ω
Wire impedance of $Z_3 = R_3 + jX_3$	0.7638 + j0.09929 Ω
Wire impedance of $Z_4 = R_4 + jX_4$	0.7638 + j0.09929 Ω
Wire impedance of $Z_5 = R_5 + jX_5$	1.5276 + j0.1986 Ω
Wire impedance of $Z_6 = R_6 + jX_6$	1.0184 + j0.1324 Ω
Wire impedance of $Z_7 = R_7 + jX_7$	1.2730 + j0. 1655 Ω
Proportional gain of PI controller	10
Integral gain of PI controller	60
Coefficient K_1 of DHOD	$3*10^2$
Coefficient K_2 of DHOD	$1.5*10^3$
Coefficient K_3 of DHOD	$1.1*10^5$
Coefficient B_i of DHOD	20

A. Simulations

Firstly, this article investigates the voltage regulation of a single CL with the injection of renewable energy current. As shown in Fig. 8(a), due to the inductive reactance of the circuit and an excessive amount of renewable energy current, the voltage amplitude across the load significantly exceeds the rated value of $220\sqrt{2}$ V. Without the power compensation of ES, the root mean square (RMS) value of voltage on the CL and NCL is 310.2 V and 311.8 V, respectively. Furthermore, the phase-*a* voltages of CL and NCL are also plotted for illustrations. The active power and reactive power borne on the CL are 12 *k*W and 8.03 *k*Var, respectively. This greatly exceeds its rated powers and can cause equipment damage.

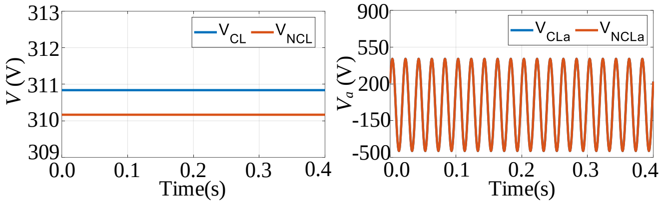

(a) (b)

Fig. 8. Voltage of CL and NCL under RES: (a) RMS value, (b) Phase-*a* voltage.

Subsequently, in Fig. 9, the ES is connected to the power grid. Initially, only power control loop is applied in the period of 0s to 0.1s. However, the reactive power output of the ES, based on the prescribed power control, was insufficient, causing the CL voltage to fall short of the rated value. Therefore, with only the power regulation loop applied, the (RMS) voltage of the CL was adjusted to 212.2 V, while the NCL and ES voltages are 146.4 V and 216.8 V, respectively. Consequently, the CL power could not reach full load, with active power at 5.6 *k*W and reactive power at 3.7 *k*Var, as depicted in Fig. 10. At 0.2 s, the proposed voltage-power control loop operates, enabling adaptive regulation of the power compensated by ES. Active power (provided by ES) decreased from 5.0 *k*W to 3.0 *k*W, and reactive power changed from -5.0 *k*Var to -6.5 *k*Var. The voltage on the NCL was regulated to 152 V, reducing consumed powers to 1.5 *k*W and 590 Var. In addition, due to appropriate power compensation in Fig. 10, the CL voltage is controlled at 220V. Meanwhile, its consumption of active and reactive power also reached the rated values, as shown in Fig. 10.

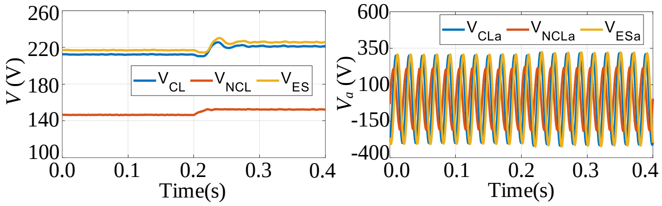

(a) (b)

Fig. 9. Voltage of CL, NCL and ES under RES: (a) RMS value, (b) Phase-A voltage.

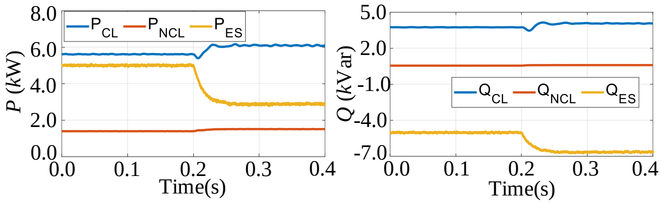

(a) (b)

Fig. 10. Powers of CL, NCL, and ES: (a) active powers, and (b) reactive powers.

Then, the consensus-based cooperative control under FDI attacks for three ESs are studied. The proposed control strategy is applied for the ESs to achieve voltage restoration based on the communication network in Fig. 7. In Fig. 11, the waveforms of bus voltages and estimated attack signals are plotted. Additionally, Figs. 12 (a) and (b) present the output active powers and output reactive powers, respectively. From 0 s to 2 s, voltage regulation for CLs is achieved through the proposed voltage-power control. At 2 s, an attack signal η = +5 is applied to ES$_2$, resulting in an increase in bus voltage (V_{ES2}) to 225 V, as evidenced in Fig. 11(a). To align with the adjusted voltage reference, the output reactive power from ES$_2$ rises to 7.9 *k*Var, while the active power decreases to 1.85 *k*W. Utilizing the reconstruction rule in (25), with B_i = 20, accurate estimation of the attack signals on ES$_2$ as +5 is achieved. Subsequently, from 10 s to 16 s, compensation for the attack signals is executed. Notably, during this period, successful restoration of bus voltages for CLs is observed. For the utilized ring network configuration, each ES in the SLs is responsible for voltage regulation and power compensation. Consequently, even if an attack induces abnormal voltage in an SL, the flow changes between SLs remain minimal.

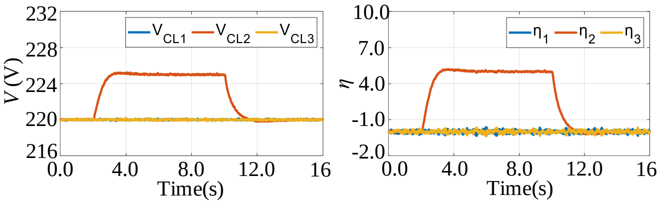

(a) (b)

Fig. 11. (a) Voltages of CLs, and (b) estimated attack signals under FDI attacks.

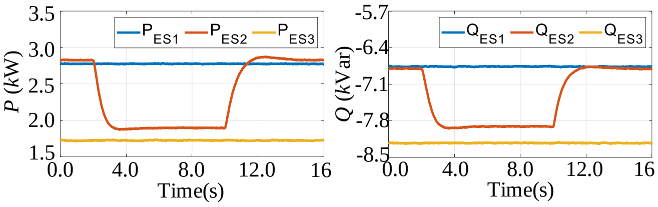

(a) (b)

Fig. 12. (a) Active powers, and (b) reactive powers of ESs under FDI attacks.

For comparison, a distributed sliding mode observer is also used to detect the state variables and FDI attacks. As shown in Fig. 13, although the sliding mode observer can estimate the attack signal, it exhibits significant chattering. Moreover, during the state observation process, the sliding mode observer requires an adjustment time of 1.5 seconds. Consequently, the dynamic response speed of the sliding mode observer has not improved compared to that of the DHOD.

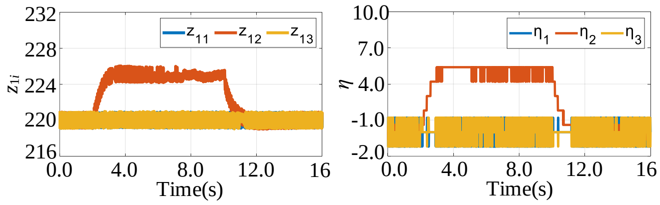

(a) (b)

Fig. 13. (a) Estimated voltages, and (b) estimated attack signals by distributed sliding mode observer.

B. *Experiments*

To further validate the effectiveness of the proposed DHOD-based cooperative control, experiments are conducted using the OPAL-RT platform, as shown in Fig. 14. The five-bus electric network, built using MATLAB with the same structure and parameters, is then executed on the RT-LAB platform. The model and algorithm are run, and the results, along with system variables, are captured via an interface board and measured with an oscilloscope.

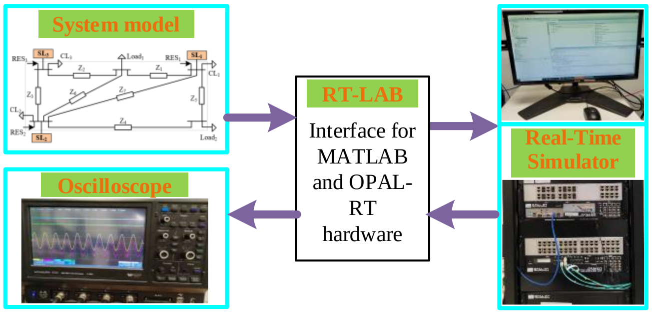

Fig. 14. OPAL-RT platform.

For experiments, this work commences by exploring voltage regulation for a singular CL under the influence of injected renewable energy current. As depicted in Fig. 15, when devoid of an ES connection, the RMS voltage levels across both the CL and NCL reach 291.4 V and 290.8 V, correspondingly. This elevation in voltage stems from the circuit's inductive reactance and an excessive influx of renewable energy current, surpassing the stipulated 220 V rating. Additionally, the CL incurs active power and reactive power consumption of 10.6 *k*W and 7.06 *k*Var, respectively, substantially exceeding their designated capacities and posing a threat of equipment damage.

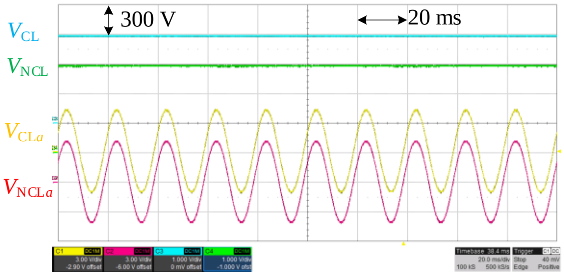

Fig. 15. Voltages of CL, and NCL under RES.

Subsequently, the ES is connected to the power grid. As shown in Fig. 16 (from 0 s to 0.5 s), when only power regulation loop was applied, the voltage of the CL was adjusted to 205 V. At the same time, the voltages on the NCL and the ES are 141.4 V and 207.8 V, respectively. However, the reactive power output of the ES based on the prescribed power control was insufficient, resulting in the voltage of the CL not reaching the rated value. As a result, the power on the CL could not achieve full load: active power is 5.23 *k*W and reactive power is 3.48 *k*Var, as shown in Fig. 17. At 0.5 s, the proposed voltage-power control loop begins functioning, allowing for adaptive adjustment of the power compensated by the ES: the active power changed from 5.0 *k*W to 2.0 *k*W, and the reactive power changed from -5.0 *k*Var to -7.7 *k*Var. The voltage on NCL is regulated to be 151.8 V, with the consumed active and reactive powers are 1.48 kW and 580 Var. Furthermore, in Fig. 16 and Fig. 17, the voltage of the CL is controlled at 220 V, and its consumption of active and reactive power also reached the rated values: 6.0 *k*W and 4.0 *k*Var.

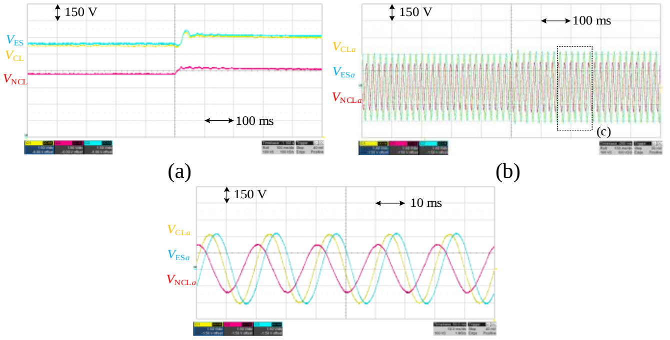

(a) (b)

(c)

Fig. 16. Voltages of CL, NCL, and ES under RES: (a) RMS values, (b) phase-A voltages, (c) phase-A voltages at short time scale.

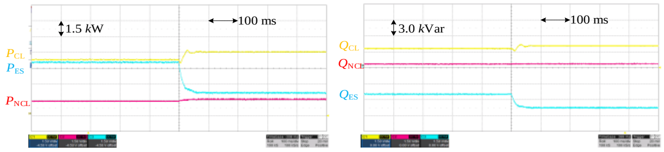

(a) (b)

Fig. 17. Powers of CL, NCL, and ES: (a) active powers, and (b) reactive powers.

For the experiments, the proposed control strategy is implemented to facilitate voltage restoration for the ESs via the communication network shown in Fig. 7. The waveforms of the bus voltages and estimated attack signals are illustrated in Fig. 18. The output active and reactive powers of the three ESs are depicted in Figs. 19(a) and 19(b), respectively. Initially, from 0 s to 10 s, voltage regulation for CLs is achieved through the proposed voltage-power control mechanism. At the 10 s, a constant attack signal (η=+5) is applied to ES$_2$, resulting in an increase in the bus voltage V_{ES2} to 225 V, as indicated in Fig. 18 (a). To align with the adjusted voltage reference, the output reactive power from ES$_2$ changes from -6.8 *k*Var to -7.9 *k*Var, while the active power decreases from 2.79 *k*W to 1.9 *k*W. Utilizing the coefficient B_i=20 for reconstructing the attack signals, according to the proposed reconstruction rule (25), the attack signals on ES$_2$ are accurately estimated as +5. Subsequently, from 35 to 50 seconds, the attack signals are effectively compensated, and the bus voltages of the CLs are successfully restored throughout this period. Unlike the parallel connection structure, a ring network structure is used here, with each ES in the SLs employed for voltage regulation and power compensation. Consequently, even if an attack causes abnormal voltage in an SL, the changes in flow between each SL remain minimal.

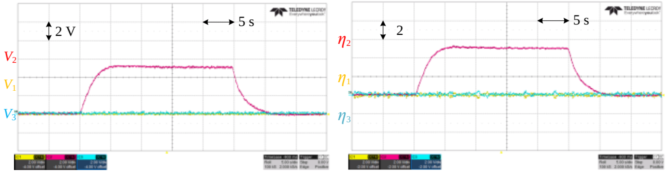

(a) (b)

Fig. 18. (a) Voltages of CLs, and (b) estimated attack signals under FDI attacks.

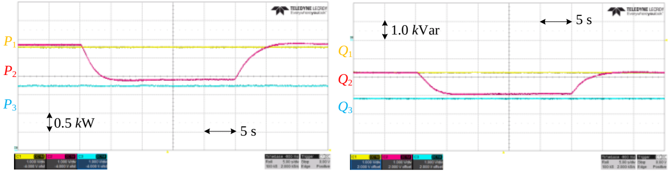

(a) (b)

Fig. 19. Powers of ESs: (a) Active powers, and (b) reactive powers.

For comparison, a distributed sliding mode observer is also used to detect the state variables and FDI attacks. As shown in Fig. 20, although the sliding mode observer can estimate the attack signal, it exhibits significant chattering. Moreover, during the state observation process, the sliding mode observer requires an adjustment time of 1.5 seconds. Consequently, the dynamic response speed of the sliding mode observer has not improved compared to that of the DHOD.

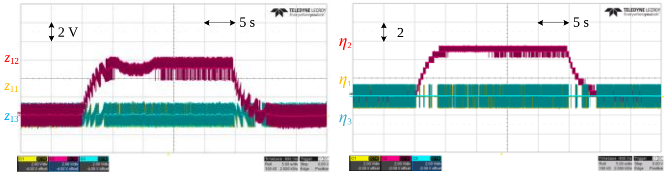

(a) (b)

Fig. 20. (a) Estimated voltages, and (b) estimated attack signals by distributed sliding mode observer.

To further verify the enhanced effect of the proposed strategy on system stability, a linearly growing attack signal η = +0.22**t* (activated at 10 s) was injected into the controller of ES$_1$. The waveforms of the bus voltages and estimated attack signals are shown in Fig. 21, while the output active and reactive powers of the three ESs are depicted in Figs. 22(a) and 22(b), respectively. Initially, from 0 s to 10 s, voltage regulation for CLs is achieved through the proposed voltage-power control mechanism. At the 10 s, the constant attack signal is applied to ES$_1$, resulting in an increase in the bus voltage V_{ES1} to 225.5 V, as indicated in Figure 21 (a). To align with the adjusted voltage reference, the output reactive power from ES$_1$ changes from -6.8 *k*Var to -7.9 *k*Var, while the active power decreases from 2.79 *k*W to 1.9 *k*W. According to the proposed reconstruction rule (25), the attack signals on ES$_2$ are accurately estimated. Subsequently, from 35 s to 50 s, the attack signal is effectively compensated, and the bus voltages of the CLs are successfully restored throughout this period. Additionally, due to the large amplitude of the attack signal, the active and reactive power outputs of the unaffected ESs are also influenced: the active power of ES2 increases, while its reactive power decreases.

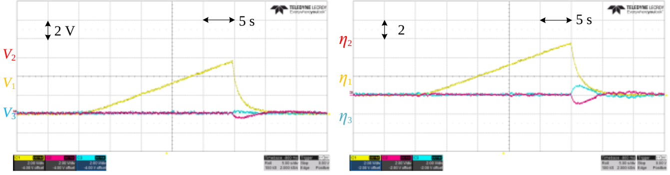

(a) (b)

Fig. 21. (a) Voltages of CLs, and (b) estimated attack signals under FDI attacks.

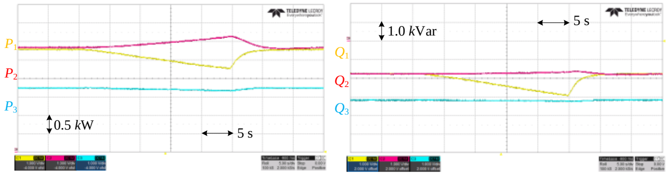

(a) (b)

Fig. 22. Powers of ESs: (a) active powers, and (b) reactive powers.

Based on the above conditions, the waveforms without observation and compensation are used to demonstrate the destructive impact of FDI attacks. The attack is activated at 5 s, and the experimental waveforms for voltages, active powers, and reactive powers are shown in Fig. 23. The figures illustrate that as the attack signal increases, the voltages and power gradually deviate from their initial values. Without detection and compensation of the attack signals, significant disruptions to the voltage stability of the entire system occur when the attack signal is large. Notable voltage oscillations are evident within 46 s, leading to fluctuations in the active and reactive power injected by each ES and ultimately resulting in system collapse.

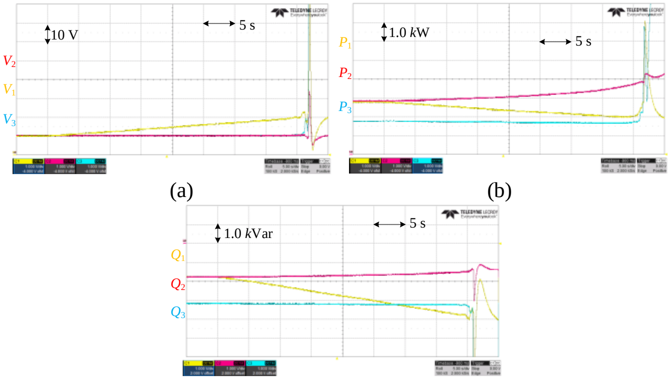

(a) (b)

(c)

Fig. 23. (a) Voltages of CLs, (b) active powers of ESs, and (c) reactive powers of ESs.

Additionally, the observation performance of the DHOD is evaluated under varying power and current injections by RES. The waveforms of the voltages and the estimated attack signal are presented in Fig. 24(a) and Fig. 24(b), respectively. At 22.5 s, a 0.5A decrease in the current injected by RES_1 caused transient voltage fluctuations, which in turn led to fluctuations in the estimated attack signal. Nevertheless, the integration of ESs and energy storage effectively mitigates these voltage fluctuations, allowing the estimated attack signal to converge to its true value. Consequently, despite the fluctuations in the observed waveform caused by changes in RES, the accuracy of the final observation results remains unaffected.

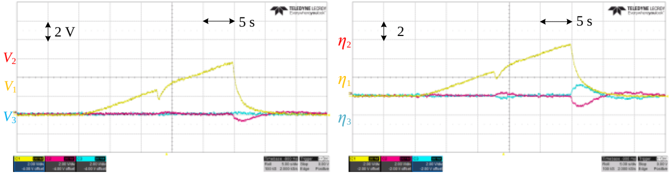

(a) (b)

Fig. 24. (a) Voltages, and (b) estimated attack signals under varying current.

V. CONCLUSION

This article introduces a solution for enhancing environmental protection and promoting battery recycling by integrating a three-phase ES system with second-life batteries. To optimize the limited output current of these batteries, a voltage feedback-based reactive power regulation strategy is employed, which ensures stability for the CLs. Furthermore, a consensus algorithm is applied to achieve voltage consensus and restoration across multiple ESs, helping to mitigate potential FDI attacks on the consensus controller. To address this vulnerability, the article utilizes a DHOD to detect and eliminate attack signals. Both simulation and experimental validations demonstrate the effectiveness of this approach in improving voltage stability and energy throughput, even in the presence of network attacks. The safe operation of power grids integrating RESs and ESs is increasingly valued. Future studies will extensively investigate analysis and detection strategies for power grid security under extreme attacks in complex power network scenarios.

ACKNOWLEDGEMENT

The authors would like to thank the financial supports from the Ministry of Education (MoE) Academic Research Fund (AcRF) Tier-1 Seed Fund RS12/23 and NTU&ICL 5th Call for Imperial-Nanyang Technological University Collaboration Fund-Open Theme 03INS001928C140.

REFERENCES

[1] K. Mok, S. Ho, S. Tan, and S. Y. R. Hui, “A comprehensive analysis and control strategy for nullifying negative- and zero-sequence currents in an unbalanced three-phase power system using electric springs,” *IEEE Trans. Power Electron*., vol. 32, no. 10, pp. 7635–7650, Oct. 2017.

[2] M. Rouholamini, C. Wang, H. Nehrir, X. Hu, Z., Hu, H. Aki, B. Zhao, Z. Miao, and K. Strunz, “A review of modeling, management, and applications of grid-connected Li-ion battery storage systems,” *IEEE Trans. Smart Grid*, vol. 13, no. 6, pp.4505-4524, Nov. 2022.

[3] Y. Mao, J. Bao, Y. Zhang, and Y. Yang, “An ultrafast variable forgetting factor recursive least square method for determining the state-of-health of Li-ion batteries,” *IEEE Access*, vol. 11, pp. 141152-141161, Dec. 2023.

[4] Y. Jiang, and Y. Yang, “A distributed proportional-integral observer-based hierarchical control for AC microgrids under FDI attacks,” *IEEE Trans. Ind. Electron.*, Early Access, May 2024.

[5] R. S. Pawar, S. P. Gawande, R. N. Nagpure, and M. A. Waghmare, “Modified instantaneous symmetrical component algorithm-based control for operating electric spring in active power filter mode,” *IET Power Electron*., vol. 12, no. 7, pp. 1730–1741, Jun. 2019.

[6] M.G. Taul, X. Wang, P. Davari, and F. Blaabjerg, “Current limiting control with enhanced dynamics of grid-forming converters during fault conditions,” *IEEE J. Emerg. Sel. Topics Power Electron*., vol. 8, no. 2, pp.1062-1073, Jun. 2020.

[7] H. Wu, and X. Wang, “Control of grid-forming VSCs: A perspective of adaptive fast/slow internal voltage source,” *IEEE Trans. Power Electron*., vol. 38, no. 8, pp. 10151-10169, Aug. 2023.

[8] M. Chen, D. Zhou, A. Tayyebi, E. Prieto-Araujo, F. Dörfler, and F. Blaabjerg, “Generalized multivariable grid-forming control design for power converters,” *IEEE Trans. Smart Grid*, vol. 13, no. 4, pp. 2873-2885, Jul. 2022.

[9] Y. Yang, S. -S. Ho, S. -C. Tan, and S. -Y. R. Hui, “Small-signal model and stability of electric springs in power grids,” *IEEE Trans. Smart Grid*, vol. 9, no. 2, pp. 857-865, Mar. 2018.

[10] Y. Yang, Y. Qin, S. -C. Tan, and S. Y. R. Hui, “Reducing distribution power loss of islanded AC microgrids using distributed electric springs with predictive control,” *IEEE Trans. Ind. Electron.*, vol. 67, no. 10, pp. 9001-9011, Oct. 2020.

[11] Q. Wang, Z. Ding, M. Cheng, F. Deng and G. Buja, “Direct power control of three-phase electric springs,” *IEEE Trans. Ind. Electron*., vol. 69, no. 12, pp. 13033-13044, Dec. 2022.

[12] F. Zhao, X. Wang, and T. Zhu, “Power dynamic decoupling control of grid-forming converter in stiff grid,” *IEEE Trans. Power Electron*., vol. 37, no. 8, pp.9073-9088, Aug. 2022.

[13] Q. Wang, M. Cheng, Y. Jiang, W. Zuo, and G. Buja, “A simple active and reactive power control for applications of single-phase electric springs,” *IEEE Trans. Ind. Electron*., vol. 65, no. 8, pp. 6291–6300, Aug. 2018.

[14] X. Chen, Y. Hou, S. -C. Tan, C. -K. Lee, and S. Y. R. Hui, “Mitigating voltage and frequency fluctuation in microgrids using electric springs,” *IEEE Trans. Smart Grid*, vol. 6, no. 2, pp. 508-515, Mar. 2015.

[15] J. Chen, A.J. Gallo, Yan, S. T. Parisini, and S.Y.R. Hui, “Cyber-attack detection and countermeasure for distributed electric springs for smart grid applications,” *IEEE Access*, vol. 10, pp.13182-13192, Feb. 2022.

[16] T. Chen, H. Liu, C.K. Lee, and S. Y. R. Hui, “A generalized controller for electric-spring-based smart load with both active and reactive power compensation,” *IEEE J. Emerg. Sel. Topics Power Electron*., vol. 8, no. 2, pp.1454-1465, Apr. 2019.

[17] L. Zhao, J. Li, Q. Li, and F. Li, “A federated learning framework for detecting false data injection attacks in solar farms,” *IEEE Trans. Power Electron.*, vol. 37, no. 3, pp.2496-2501, Mar. 2022.

[18] J. Chen, S. Yan, T. Yang, S.C. Tan, and S.Y.R. Hui, “Practical evaluation of droop and consensus control of distributed electric springs for both voltage and frequency regulation in microgrid,” *IEEE Trans. Power Electron*., vol. 34, no. 7, pp.6947-6959, Jul. 2019.

[19] D. Qiu, C. Yuan, B. Zhang, M. Ke, Y. Chen, and F. Xie, “An improved electric spring topology based on LCL filter,” *IEEE Trans. Power Electron*., vol. 37, no. 5, pp.5984-5994, May 2022.

[20] Z. Xie and Z. Wu, “Distributed fault-tolerant secondary control for DC microgrids against false data injection attacks,” *Int. J. Electr. Power Energy Syst*., vol. 144, Article ID 108599, 2023.

[21] J.A.C. González, O. Salas-Peña, and J. De León-Morales, “Observer-based super twisting design: A comparative study on quadrotor altitude control,” ISA Transactions, vol. 109, pp. 307-314, Mar. 2021.

[22] J. Zhang, S. Sahoo, J. C. Peng, and F. Blaabjerg, “Mitigating concurrent false data injection attacks in cooperative dc microgrids,” *IEEE Trans. Power Electron*., vol. 36, no. 8, pp. 9637-9647, Aug. 2021.

[23] R. Ma, Z. Hu, H. Yang, Y. Jiang, M. Huo, H. Luo, and R. Yang, “Adversarial FDI attack monitoring: Toward secure defense of industrial electronics,” *IEEE Ind. Electron., Mag*., vol. 18, no. 2, pp. 48-57, Jun. 2024.

[24] R. Razi, H. Iman-Eini, and M. Hamzeh, “An impedance-power droop method for accurate power sharing in islanded resistive microgrids,” *IEEE J. Emerg. Sel. Topics Power Electron.*, vol. 8, no. 4, pp. 3763-3771, Dec. 2019.

[25] Y. Jiang, Y. Yang, S. C. Tan and S. Y. R. Hui, “Distributed sliding mode observer -based secondary control for DC microgrids under cyber-attacks,” *IEEE, J. Emer. Sel. Top. Circuits Syst*., vol. 11, no. 1, pp. 144-154, Mar. 2021.

[26] Y. Chen, D. Qi, H. Dong, C. Li, Z. Li, and J. Zhang, “A FDI attack-resilient distributed secondary control strategy for islanded microgrids,” *IEEE Trans. Smart Grid*, vol. 12, no. 3, pp.1929-1938, May 2021.

[27] Y. Zuo, J. Chen, X. Zhu, and C.H. Lee, “Different active disturbance rejection controllers based on the same order GPI observer,” *IEEE Trans. Ind. Electron.*, vol. 69, no. 11, pp. 10969-10983, Nov. 2021.

[28] S. Jena, A. Mishra, and N.P. Padhy, “Cyber-secure global operation of grid forming inverters in pinning-based AC microgrid clusters,” *IEEE Trans. Ind. Appl*., Early Access, Jul. 2024.

[29] C. Fu, C. Zhang, G. Zhang, and L. Xing, “Distributed fast finite-time secondary control of islanded microgrids: A disturbance observer-based approach,” *Int. J. Electr. Power Energy Syst.*, vol. 157, p.109813, Jan. 2024.

[30] Y. Jiang, Y. Yang, S. C. Tan, and S. Y. R. Hui, “A high-order differentiator based distributed secondary control for DC microgrids against false data injection attacks,” *IEEE Trans. Smart Grid*, vol. 13, no. 5, pp. 4035 – 4045, Sept. 2022.

[31] W. Vermeer, G.R.C. Mouli, and P. Bauer, “A comprehensive review on the characteristics and modeling of lithium-ion battery aging,” *IEEE Trans. Transport. Electrific*., vol. 8, no. 2, pp.2205-2232, Jun. 2022.

[32] Q. Su, H. Fan, and J. Li, “Distributed adaptive secondary control of AC microgrid under false data injection attack,” *Electric Power Systems Research*, vol. 223, p.109521, Oct. 2023.

Yajie Jiang (Member, IEEE) received the B.Eng. degree in electrical engineering from the School of Electrical Engineering, Zhengzhou University, Zhengzhou, China, in 2015, the M.Eng. degree in electrical engineering from the School of Electrical and Electronic Engineering, Huazhong University of Science and Technology, Wuhan, China, in 2018, and the Ph.D. degree in electrical engineering from the Department of Electrical and Electronic Engineering, The University of Hong Kong, Hong Kong, China, in 2022. He is currently a Research Fellow with the School of Electrical and Electronic Engineering, Nanyang Technological University, Singapore. His research interests include power electronics, smart grid, and machine drives.

Xiangrong Zhang received his bachelor's degree in electrical engineering from South China University of Technology in 2023. He is now pursuing a master's degree in electrical engineering at Nanyang Technological University, focusing his research on power electronics.

Yici Wang is currently pursuing his bachelor's degree in electrical engineering at Nanyang Technological University. Her research interest is the power electronics in power systems.

Yunjie Gu (M’18-SM’20) received the B.Sc. and the Ph.D. degree in electrical engineering from Zhejiang University, Hangzhou, China, in 2010 and 2015 respectively. He is now a Lecturer at Imperial College London, where he was an EPSRC funded Innovation Fellow (award EP/S000909/1). Before his academic career, he was a Consulting Engineer at General Electric Global Research Centre, Shanghai, China. His research interests include stability theory for inverter-based power systems, stability-enhancing inverter technologies, and numerical methods for computer-aided stability analysis.

Ka-wai Eric Cheng (Fellow, IEEE) received the B.Sc. and Ph.D. degrees from the University of Bath, Bath, U.K., in 1987 and 1990, respectively. Before joining The Hong Kong Polytechnic University, Hong Kong, in 1997, he was with Lucas Aerospace, London, U.K., as a Principal Engineer. He is currently a Professor, Department of Electrical Engineering, School of Engineering, University of California, Merced. He has authored or co-authored more than 400 articles and seven books. His research interests include all aspects of power electronics, motor drives, electromagnetic interference, electric vehicles, battery management, and energy saving.

Yun Yang (M’18-SM’23) research interests include wireless power transfer, renewable energy technologies, electric vehicles, power electronics, and advanced control. received the B.Sc. degree in electrical engineering from Wuhan University, Wuhan, China, in 2012, and the Ph.D. degree in electrical engineering from The University of Hong Kong, Hong Kong, in 2017. He was a Research Assistant Professor with the Department of Electrical Engineering, The Hong Kong Polytechnic University. He is currently an Assistant Professor with the School of Electrical and Electronic Engineering, Nanyang Technological University, Singapore. His research interests include power electronics, wireless power transfer, battery storage technologies, and smart grid systems.